# 电弧喷涂铁基非晶涂层的结构与性能

傅斌友[1,2], 贺定勇[1], 赵力东[2], 李晓延[1]
(1. 北京工业大学 材料科学与工程学院, 北京 100124;
2. 德国亚琛工业大学 表面工程研究所, 德国 亚琛 52062)

傅斌友

摘 要: 用电弧喷涂技术在低碳钢基体上制备一种含非晶和纳米晶的 Fe 基涂层. 采用 X 射线衍射仪(XRD)、扫描电镜(SEM)、透射电镜(TEM)、显微硬度仪分析测量涂层的组织和性能. 并用谢乐公式计算晶粒尺寸. 结果表明, 涂层呈典型的层状组织结构, 由变形良好的带状粒子相互搭接堆积而成. 涂层结构致密, 孔隙率低, 氧化物含量较少, 涂层含有非晶和纳米晶, 晶粒尺寸为 10~40 nm, 利用 X 射线衍射强度比较法测量涂层中非晶相的含量为 55.3%. 涂层具有很高的硬度, 其显微硬度最高达到 1 260 HV0.1.

关键词: 非晶; 纳米晶; 电弧喷涂; 组织与性能
中图分类号: TG172 文献标识码: A 文章编号: 0253-360X(2009)04-0053-04

## 0 序 言

非晶态金属合金作为一种新型材料, 不仅具有极高的强度、韧性、耐磨性和耐蚀性, 而且还表现出优良的软磁和硬磁性能、超导特性及低磁损耗等特点[1], 是当前国际材料研究的热点之一; 利用非晶态合金制备优异的耐磨耐腐蚀防护涂层也成为当前材料表面防护的热点研究课题之一. 目前, 国内外研究人员利用多种方法来制备非晶涂层, 热喷涂技术制备表面非晶涂层就是对非晶合金制备技术的新开拓. Shmyreva 等人[2] 利用爆炸喷涂方法(DGS)制备了 Fe-Cr-P-C 非晶, Kobayashi 等人[3] 利用智能等离子喷涂方法(SPS)制备了铁基非晶涂层, Dent 等人[4] 利用高速氧燃料喷涂(HVOF)制备的 Ni-Cr-B-C 涂层中含有非晶相. Choi 等人[5] 报道了 Ni-Zr-Ti-Si-Sn 非晶金属涂层可由真空等离子喷涂方法(VPS)制备. 国内郭金花等人[6] 利用电弧喷涂(AS)方法制备了含部分非晶相的铁基涂层, 并研究了涂层组织和电化学性能. 与其它热喷涂方法相比, 电弧喷涂由于设备简单、可以现场原位大面积喷涂、涂层性能优异和具有优良的经济性等特点而被广泛应用, 利用电弧喷涂制备非晶涂层不仅具有广阔的应用背景, 还可为研究其形成机理、组织结构及性能提供良好的依据.

收稿日期: 2008-07-07
基金项目: 德国科学基金会(DFG)资助项目(ZH 205/1-1)
German science foundation (DFG) within the scope of the project (ZH205/1-1)

文中利用电弧喷涂方法喷涂粉芯丝材制备了 Fe 基非晶涂层, 通过 Verdon 方法[7] 对 XRD 衍射图进行 Pseudo-Voigt 函数[8] 拟合, 计算了涂层中非晶相含量, 利用谢乐公式计算晶粒尺寸, 并对非晶涂层的组织和性能进行了研究, 为后续深入研究其形成机理、组织结构及性能提供良好的依据.

## 1 试验方法

试验采用 JZY-250 型电弧喷涂设备制备涂层. 喷涂材料为自制的 Fe 基粉芯丝材, 直径2.0 mm, 其主要化学成分(质量分数, %): Fe49.64, Cr38.05, Ni5.44, B4.24, C1.15. 基体材料为 Q235 低碳钢, 尺寸为 57 mm×25 mm×5 mm, 表面经喷砂处理后喷涂 1.0 mm 厚的涂层, 喷涂过程中未使用冷却气. 优化喷涂工艺参数为: 电压 28 V, 电流 180 A, 压缩空气压力 0.55 MPa, 喷涂距离 250 mm.

采用 D8 ADVANCE 型 X 射线衍射仪(XRD)对涂层进行物相分析, 衍射条件为 CuKα 靶, 40 kV 和 20 mA. 采用 FEI Quanta 200 型扫描电子显微镜(SEM)观察涂层磨损后形貌. 采用 JEM-2000FX 型透射电子显微镜(TEM)观察涂层中的非晶相. 采用图像分析软件测量涂层孔隙率, 孔隙率取 10 点平均值.

采用 Micronmet1 显微硬度仪测量试样显微硬度, 硬度值测试区域为涂层侧面中间位置, 载荷为 0.98 N, 试验结果取 10 点平均值. 涂层热处理温度为 600 ℃, 保温时间为 1 h, 空冷.

## 2 结果与讨论

### 2.1 涂层的形貌

图1为电弧喷涂 Fe 基非晶涂层截面的微观形貌，涂层由变形良好的带状粒子相互搭接堆积而成，呈典型的层状结构形貌. 这是因为在电弧喷涂过程中绝大部分雾化粒子以熔化或部分熔化的状态撞击到了基体上，粒子铺展良好，迅速沉积固化，从而形成了层状搭接结构. 由图 1 可以发现，涂层由不同的层状组织组成，形成这种不均匀结构的主要原因是因为在电弧喷涂过程中丝材端部熔化，经压缩空气雾化成大小不同的熔滴，熔滴加速撞击到基体时就会形成形状不同的层状组织. 涂层中白色区域为基体组织（图 1 中 A），灰色区域为氧化物（图 1 中 B）. 从图 1 中可以发现，这些氧化物呈薄片状，连续分布于白色基体相的界面处. 涂层中层与层之间结合致密，孔隙较少，通过图像分析软件测量涂层平均孔隙率为 2.33%.

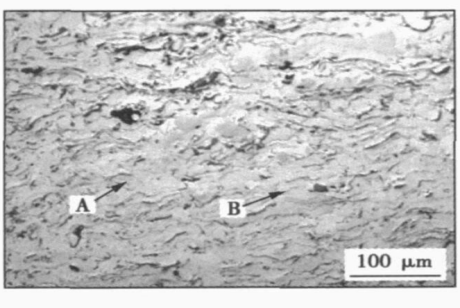


图 1 涂层截面显微组织

Fig. 1 Cross-section of coating

### 2.2 涂层的相组成

图2为非晶涂层X射线衍射图谱，图谱中45°左右存在明显的非晶包，由此可以证明涂层中存在非晶相. 通过 Verdon 方法对 XRD 衍射图进行 Pseudo-Voigt 函数拟合，拟合曲线如图 2b 所示. 涂层中非晶含量利用衍射强度法计算[9]，计算结果得出非晶涂层的非晶相含量为 55.3%. 由图 2a 可以发现，XRD 图谱中除了表征非晶相的漫散射包，同时还出现了部分晶体相的衍射峰，涂层中的晶体相为 (Fe, Cr)，$Fe_2B$，$M_{23}(C,B)_6$ 和 $Cr_2B$.

分析认为非晶涂层中出现晶体相的主要原因是因为电弧喷涂是一个快速熔化、雾化、凝固过程，熔滴合金成分不均匀，因而生成的涂层结构也不均匀，不能形成完全的非晶块体. 另一方面，电弧喷涂过程是在大气中进行，熔融液滴不可避免的发生氧化，

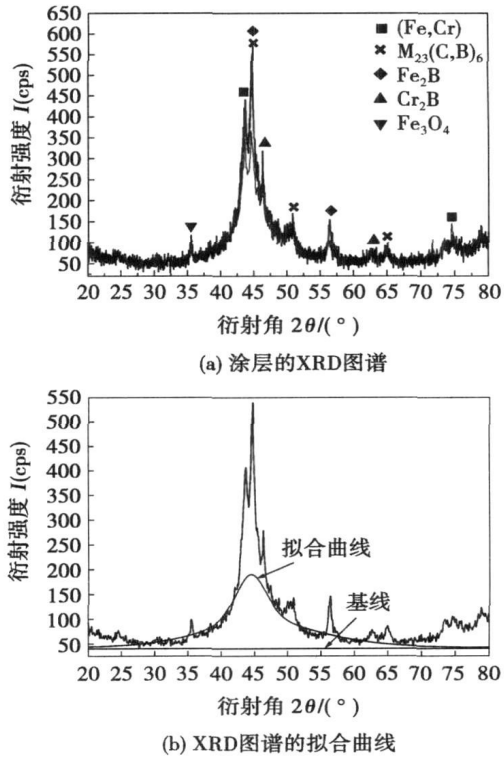


图 2 涂层的 XRD 图谱及其拟合曲线

Fig. 2 XRD spectra of coating and its fitting curve

也影响了非晶的形成能力. 观察图 2a 可以发现两个主峰并不尖锐，这说明涂层中的晶体相晶粒细小，根据谢乐公式计算（Fe, Cr）相平均晶粒尺寸为 23 nm，$Fe_2B$，$M_{23}(C,B)_6$ 相平均晶粒尺寸为 30 nm. 除了 (Fe, Cr) 和 $M_{23}(C,B)_6$ 晶体相外，涂层中还存在 $Fe_2B$，$Cr_2B$ 硬质相，Fe，Cr 为过渡族金属，硼为类金属，电负性相差较大，二者容易结合形成间隙化合物. 硼化物的硬度高，在磨损过程中可以起到耐磨骨架的作用，能显著地提高涂层的耐磨性.

### 2.3 涂层的微观形貌

为了进一步证明涂层中存在非晶、纳米晶，将涂层减薄，进行透射电镜观察试验. 图 3 为涂层透射电镜照片，由图 3 可知，涂层由非晶、纳米晶组成，纳米晶均匀弥散分布于非晶之中. 纳米晶在外界提供的热量作用下长大，各微区的加热程度不同，纳米晶的尺寸也不同，一般为 10～30 nm，这个结果跟谢乐公式计算结果相一致. 关于涂层中同时存在非晶与纳米晶的原因可以做如下解释：非晶态在热力学上是一种亚稳状态，其自由能比相应的晶体高，在一定条件下，有降低能量转变成晶体的趋势. 电弧喷涂过程中，尽管涂层与基体的总体温度低，但由于涂层是一层层堆积而成，喷涂过程中后续涂层产生的热量作用于前一涂层，相当于对已形成的非晶进行了

退火，其热影响可局部超过非晶晶化温度，因此容易形成纳米晶．同时，喷涂液滴固化释放的结晶潜热也为纳米晶的形成提供了部分热量．

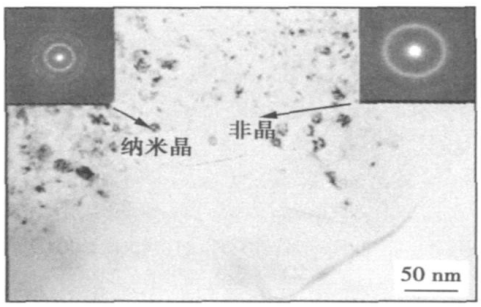


图 3　涂层的 TEM 形貌及选取衍射花样

Fig. 3　TEM morphology and electronic diffraction pattern of coating

## 2.4　涂层的 DTA 曲线

为了研究涂层中非晶的晶化温度，对涂层做了差热分析试验．图 4 为涂层的 DTA 曲线，由图 4 看出，在 566 ℃左右存在一个放热峰，表明了涂层的晶化温度为 566 ℃．为了验证这一结果，对涂层在 600 ℃进行热处理，保温时间 1 h，空冷，热处理后涂层的 XRD 图谱如图 5 所示．由图 5 可知，涂层经 600 ℃热处理后，非晶包完全消失，说明涂层中非晶相完全晶化，同时晶体相的衍射峰更加尖锐，说明涂层中晶体相晶粒长大．

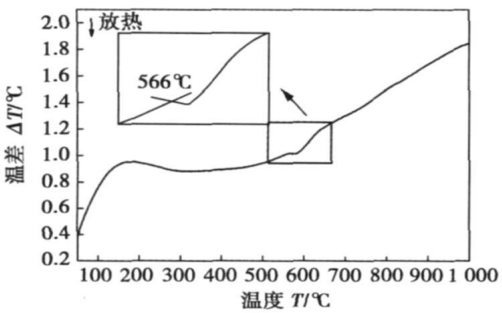


图 4　涂层的 DTA 曲线

Fig. 4　DTA spectrum of coating

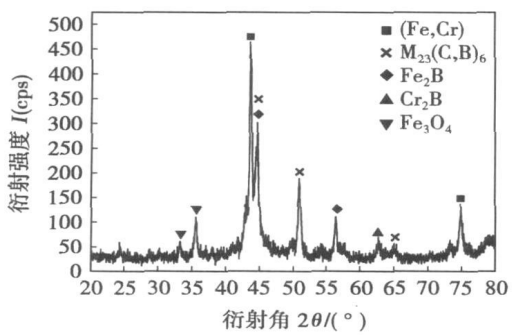


图 5　涂层经 600 ℃热处理后的 XRD 图谱

Fig. 5　XRD pattern of coating annealed at 600 ℃

## 2.5　涂层硬度分析

在平行于电弧喷涂方向截取截面，对涂层的显微硬度进行分析，涂层的显微硬度超过了 900 HV0.1，属于硬质涂层．这主要是因为涂层中含有非晶相和 $Fe_2B$，$Cr_2B$ 硬质相，此外涂层在形成时高速撞击基体并激冷，部分晶粒细化以及晶格产生畸变使涂层得到强化．由图 6 可知，基体硬度在 150 ~ 200 HV0.1 范围内，在接近基体与涂层界面处硬度有增大趋势，这主要是由于在喷涂过程中基板局部发生了塑性变形，对基板起到了加工硬化作用，提高了基体局部硬度．涂层厚度小于 600 μm 时，其硬度趋于稳定，保持在 860 ~960 HV0.1 范围内，当涂层厚度大于 600 μm 时，涂层硬度呈显著增长趋势，最大硬度达到 1 260 HV0.1．分析认为厚度小于 600 μm 时，涂层组织主要为非晶相，其硬度在 860 ~ 960 HV0.1 范围内．但由于涂层是一层层堆积而成，喷涂过程中后续涂层对前一涂层有热影响，在连续喷涂且不加冷却气体保护过程中，这种热影响程度会增加，当涂层厚度大于 600 μm 时，其热影响可局部超过非晶晶化温度而形成纳米晶．因而涂层硬度呈增长趋势，最大硬度达到 1 260 HV0.1．

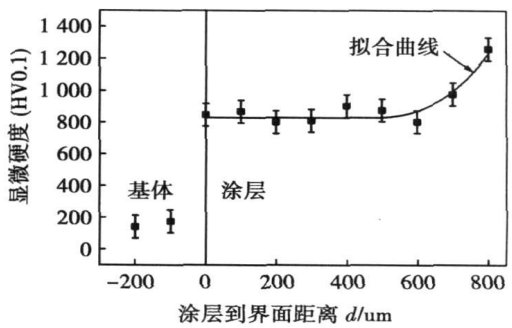


图 6　涂层的显微硬度

Fig. 6　Microhardness of coating

# 3　结　　论

（1）采用电弧喷涂方法制备 Fe 基涂层，涂层呈典型层状组织结构，结构致密，孔隙率低．

（2）采用电弧喷涂方法制备 Fe 基涂层，涂层中非晶与纳米晶共存，利用 X 射线衍射强度比较法测量涂层中非晶相的含量为 55.3%．

（3）制备的 Fe 基非晶涂层硬度高，涂层显微硬

度值在 860 ~ 1 260 HV0.1 之间, 当涂层厚度大于 600 μm 时, 显微硬度值显著增高.

参考文献:


[1] Luborsky F E. Amorphous Metallic Alloys [M]. London, Boston: Butterworths, 1983.

[2] Shmyreva T P, Mukhina L V. Formation behaviour of new amorphous and composite materials in detonation gun and plasma spraying[C] // Proceedings of the 7th National Thermal Spray Conference. Boston, Massachusetts, 1994, 201—204.

[3] Kobayashi A, Yano S, Kimur H, *et al*. Fe-based metallic glass coatings produced by smart plasma spraying process[J]. Materials Science and Engineering B, 2008, 148(1—3): 110—113.

[4] Dent A H, Horlock A J, Mccartney D G, *et al*. Microstructural characterisation of a Ni-Cr-B-C based alloy coating produced by high velocity oxy-fuel thermal spraying[J]. Surface Coating & Technology, 2001, 139(2—3): 244—250.

[5] Choi H, Yoon S, Kim G, *et al*. Phase evolutions of bulk amorphous NiTiZrSiSn feedstock during thermal and kinetic spraying processes [J]. Scripta Materialia, 2005, 53(1): 125—130.

[6] 郭金花, 吴嘉伟, 倪晓俊, 等. 电弧喷涂含非晶相的 Fe 基涂层的电化学行为[J]. 金属学报, 2007, 43(7): 780—784.
Guo Jinhua, Wu Jiawei, Ni XiaoJun, *et al*. Electrochemical behavior of Fe-based coatings containing amorphous phase prepared by electric arc spraying[J]. Acta Metallurgica Sinica, 2007, 43(7): 780—784.

[7] Verdon C, Karimi A, Martin J L. A study of high velocity oxy-fuel thermally sprayed tungsten carbide based coatings. part 1: microstructures[J]. Materials Science and Engineering A, 1998, 246(1—2): 11—24.

[8] Cerqueiraa M F, Ferreiraa J A, Adriaenssen G J. Structural studies and influence of the structure on the electrical and optical properties of microcrystalline silicon thin films produced by RF sputtering[J]. Thin Solid Films, 2000, 370(1—2): 128—136.

[9] Wang B C, Chang E, Lee T M, *et al*. Changes in phases and crystallinity of plasma 2 sprayed hydroxyapatite coatings under heat treatment: a quantitative study[J]. Journal of Biomedical Materials Research, 1995, 29(12): 1483—1492.



作者简介: 傅斌友, 男, 1980 年出生, 博士. 主要从事表面防护、热喷涂领域工作. 发表论文 10 篇.

Email: binyou@emails.bjut.edu.cn


[上接第 52 页]


[4] Casalino G, Dattoma V, Ludovico A, *et al*. The use of discharge energy for rapid welding[C] // 14th DAAAM International Symposium, Vienna, Austria, 2003.

[5] Wilson R D. Explore the potential of capacitor discharge welding[J]. Advanced Materials and Processes, 1994(145): 93—94.

[6] Takaki K, Fujimaki Y, Takada Y, *et al*. A capacitor discharge technique with optimized energy for joining ceramics[J]. Materials Science and Engineering A, 2002(65): 457—462.

[7] 翟秋亚, 徐锦锋. Cu-Sn 合金急冷箔储能焊接头的形貌特征与形成机制[J]. 金属学报, 2005, 41(7): 755—758.
Zhai Qiuya, Xu Jinfeng. Morphological characteristic and formation mechanism of joint of melt-spun Cu-Sn alloy foils by capacitor dicharge welding[J]. Acta Metallrugica Sinica, 2005, 41(7): 755—758.

[8] 徐锦锋, 魏炳波. 急冷快速凝固过程中液相流动与组织形成的相关规律[J]. 物理学报, 2004, 53(6): 160—166.
Xu Jinfeng, Wei Bingbo. Liquid phase flow and microstructure formation during rapid solidification[J]. Acta Phsica Sinica, 2004, 53(6): 160—166.

[9] 翟秋亚, 张 兴, 徐锦锋. 急冷 Ni-Si 合金箔快速凝固连接接头组织分析[J]. 焊接学报, 2007, 28(9): 99—102.
Zhai Qiuya, Zhang Xing, Xu Jinfeng. Analysis of joint microstructure of melt-spun Ni-Si alloy foils by rapid solidification joining process[J]. Transactions of the China Welding Institution, 2007, 28(9): 99—102.



作者简介: 翟秋亚, 女, 1963 年出生, 硕士, 副教授. 主要研究方向为先进材料的焊接. 发表论文 50 余篇.

Email: qiuyazhai@xaut.edu.cn

perature distributions of different scanning modes are studied and analyzed. Based on the experimental and simulation results circle scanning orderly with degressive radius from outer to inner is suitable to produce a certain width cylinder, while small electron beam current can reach temperature above the melting point. And the scanning range is consistent with the melting scope, melted powder in the depth is almost the same for the entire scanning area, so the prototyping result is uniform and the surface is flat. The temperature field of multi-layered scanning with element birth and death is predicted by simulation, and the simulation result is useful to instruct practical prototyping.

**Key words**: electron beam rapid prototyping; element birth & death; temperature field simulation

**Mathematical model of the distribution of spot welding temperature field based on current skin effect** TANG Yuanzhi (Mechanical department, Hubei Institute of Automotive Industries, Shiyan 442002, Hubei, China). p38—40

**Abstract**: In this paper, mathematical model of temperature field was set up through the heat conduction equation in the current skin effect. This process of solving was simplified, the results are accurate, the physical meanings are clear and directviewing. The results show that spot weld nugget is oval-shaped, therefore the current skin effect enlarges the spot welding area, thus increases its solidity and helps to curb the explosion of the spot weld nugget and splash. The results indicate that by changing the current frequency to adjust thickness of the current trend skin, the size of the spot weld nugget can be regulated. Under the guidance of the theory, the quality of the spot weld nugget can be improved, the structure of electrode is optimized and new weld machine is developed. The theoretical result has a great value in the engineering practice.

**Key words**: spot welding; curren skin effect; temperature distribution; spot weld nugget

**Weld seam formation control of root pass for pipeline MIG welding based on an embedded DSP visual servo platform** HUANG Cao[1], SUN Zhenguo[1], CHEN Qiang[1], LIAO Jianxiong[2], WANG Dinghe[2], CHEN Weizhong[2] (1. Key Laboratory for Advanced Materials Processing Technology, Department of Mechanical Engineering, Tsinghua University, Beijing 100084, China; 2. Huaheng Welding Equipment &Technical Co. Ltd. Kunshan 215301, Jiangsu, China). p41—44

**Abstract**: In the root pass of pipeline MIG welding, the unpredicted gap variation of weld seam caused by groove-preparing or welding deformation has extremely significant influence on the quality of weld seam. For this reason, a weld seam formation control system based on an embedded DSP (digital signal processor) visual servo platform was established. In the visual servo platform, TMS320DM642 has been used to grab and process the image in the weld pool area and TMS320F2812 has been used to accomplish real-time adjusting of welding torch posture and welding parameters. With a particularly designed image processing algorithm, the position information of weld pool, the weld seam and feeding wire were detached and calculated successfully. Then, according to the visual sensing results of weld seam width, real-time control of weld seam formation of root pass of pipeline MIG welding was fulfilled through the online regulation of welding parameters. X-ray test qualified weld seams with good apperearance are obtained.

**Key words**: root pass MIG welding; visual servo; embedded DSP system; image of weld pool area; image processing

**Mechanical properties of 1420 aluminum-lithium alloy friction stir welding** GUO Xiaojuan, LI Guang, DONG Chunlin, LUAN Guohong (China FSW Center, Beijing Aeronautical Manufacturing Technology Research Institute, Beijing 100024, China). p45—48

**Abstract**: The friction stir welding of 2.8 mm thick 1420 aluminum-lithium alloy was conducted. The mechanical property and microstructure of the joints as well as the influences of welding parameters were investigated. The results show that if the welding parameters are optimal, the tensile property and elongation of the joints can reach to 90% that of the base metal, and the higher heat input could improve the mechanical properties. SIM and microhardness analysis indicate that fracture surface was characterized by main cleavage and dimples. Compared with other area, the hardness in weld was higher, and the highest area was in the center of the weld. The maximum is the TMAZ area at the retreating sides. The microstructure behaves the 'S' characteristic.

**Key words**: friction stir welding; aluminum-lithium alloy; mechanical property; microstructure

**Microstructural characteristic of rapid solidification welding joint of melt-spun Cu-Sn peritectic alloy foils** ZHAI Qiuya, YANG Jinshan, XU Feng, XU Jinfeng (School of Materials Science and Engineering, Xi' an University of Technology, Xi' an 710048, China). p49—52, 56

**Abstract**: The rapid solidification welding of melt-spun Cu-$x$%Sn ($x$= 7, 13.5, 20) alloy foils is conducted by a micro-type capacitor discharge welding machine and the microstructural morphology of joint is investigated. The cooling rate of micro nugget is calculated and the formation of porosity in nugget is analyzed theoretically. The results indicate that the capacitor discharge welding can realize the rapid solidification welding of melt-spun Cu-Sn alloy foils. The microstructure of joint is characterized by rapid solidification which consists of fine and homogeneous equiaxed grains. The cooling rate of nugget is up to $10^7$ K/s and the welding period is merely 15.5 μs. Therefore, the joint microstructure is in accordance with the rapidly solidified alloy foils. The main welding defect is porosity. With the increase of Sn content, the porosity of nugget increases.

**Key words**: melt-spun Cu-Sn peritectic alloy foils; rapid solidification welding; microstructure of joint

**Microstructure and properties of arc sprayed coatings containing Fe-based amorphous phase** FU Binyou[1,2], HE Dingyong[1], ZHAO Lidong[2], LI Xiaoyan[1] (1. College of Materials Science and Engineering, Beijing University of Technology, Beijing 100124,

China; 2. Surface Engineering Institute, RWTH Aachen University, Yachen 52062, Germany). p53—56

**Abstract**: In the present study, a Fe-based cored wire was used to deposit coatings containing Fe-based amorphous phase and fine crystallites on a mild steel substrate by arc spraying. The microstructure and properties of coatings were investigated by XRD, SEM, TEM and micro-hardness meter; and the grain size of the coatings was determined from the corresponding peak via the Scherrer formula. The experiment results show that the coating has homogenous laminated microstructure and contains only a little micro-pores and oxides, Fe-based amorphous phase and nanocrystalline grains are observed in the coating, and the grain size of the crystalline is between 10—40 nm. The volume content of the amorphous phase in the coating amounts to 55.3% by the X-ray diffraction intensity curve. The coating is hard, with microhardness value about 1 260 HV0.1.

**Key words**: amorphous; nanocrystallite; arc spraying; microstructure and properties

**Effects of TLP bonding temperature on the microstructurs and properties of T91 joint with two-step heating process** CHEN Sijie[1,2], GE Liling[2], JING Xiaotian[2] (1. School of Materials Science & Engineering, Henan Polytechnic University, Jiaozuo 454003, Henan, China; 2. School of Materials Science & Engineering, Xi'an University of Technology, Xi'an 710048, China). p57—60

**Abstract**: A modified 9Cr-1Mo (martensitic T91 steel pipes) were joined by transient liquid-phase bonding with two-step heating process using FeNiCrSiB (A) filler in argon atmosphere. The tensile strength and bend properties of the TLP joint were examined at room temperature. The microstructures and the element distributions as well as hardness of the joints with TLP two-step heating process were also investigated by means of SEM, EPMA and microhardness meter. The testing results indicate that the temperature gradient of TLP two-step heating process has prodigious effect on microstructures and properties of the joint. The microstructures and properties of TLP joint are best with the process at 1 270 ℃ heating for 0.5 min, and at 1 230 ℃ isothermal for 3 min.

**Key words**: T91; TLP bonding; isothermal temperature; two-step heating; microstructure

**Microstructure of liquid and solid diffusion bonding region of carbon steel-brass interlayer-stainless steel** CHEN Rushu, ZHANG Fenggang, LIU Deyi, LIU Shicheng (School of Materials Science and Engineering, Dalian Jiaotong University, Dalian 116028, Liaoning, China). p61—64

**Abstract**: Microstructure of the liquid and solid diffusion bonding region of low carbon steel-H62 brass interlayer-304 stainless steel was examined by means of scanning electron microscope (SEM), energy dispersive X-ray detector (EDX) and X-ray diffractometer (XRD). Metallurgical bonding of carbon steel with stainless steel was achieved through liquid and solid diffusion at carbon steel-brass-stainless steel interfaces. Cu and Zn atoms in the liquid brass diffused through the brass/stainless interface notably, and the formed austenite was surrounded by reticulated brass. On the other hand, solid phase dissolution predominated at carbon steel/brass interface. A kind of island-form iron-rich phase, which contains chromium and nickel, was formed and distributed in brass matrix. And the iron-rich phase remained austenite when cooling to room temperature.

**Key words**: stainless steel/carbon steel; brass interlayer; liquid/solid diffusion; bonding region; iron-rich phase

**Investigation on compactness of weld in brazing copper with Cu-P amorphous fillers** YU Weiyuan, CHEN Xueding, LU Wenjiang (State Key Laboratory of Advanced Non-ferrous Metal Materials, Lanzhou University of Technology, Lanzhou 730050, China). p65—68

**Abstract**: The amorphous fillers with the components $Cu_{68.5}Ni_{15.7}Sn_{9.3}P_{6.5}$ (wt%) was used to braze copper by vacuum brazing. The compactness of joint was studied by means of XRD, EPMA and metalloscope. The results show that the main reason of brazing porosity is the vaporization of P element. Comparing of the porosity sensitivity between crystal FM and amorphous FM, it can been found that amorphous FM is better than the crystal FM. Based on the vacancy theory and the automic vibration theory, it is concluded that the porosity sensitivity is result from the high element-liveness in the fillers.

**Key words**: copper; vacuum brazing; compactness; porosity

**Study on tensile properties of friction-stir-welded joints of 2024-M aluminum alloy** JIN Yuhua, WANG Xijing, LI Changfeng, ZHANG Jie (State Key Laboratory of Advanced Non-ferrous Metal Materials, Lanzhou University of Technology, Lanzhou 730050, China). p69—72

**Abstract**: In this paper, the effect of stiring pin rotation speed on mechanical properties of 2024-M joints of friction stir welding was analysed. The results showed that the fracture position of 2024-M joints varied with the rotation speed of stiring pin in the axial tensile experiment. A larger percent of block particles were reserved in the nugget zone with higher rotation speed, the properties of welding joints decreased and the fracture occured in stir zone. With lower rotational speed, the proportion of friction mechanism between the shoulder and top surface of welded material decreased. The layered metal flow was obtained at the rotational and traverse speeds of 600 r/min and 20 mm/min respectively, and it can become lower for welding joints again. The optimal welding parameters were the rotational and traverse speeds of 800—1 200 r/min and 20 mm/min respectively. Tensile fracture surface inclined at 45° to stress axis in base metal region, which is a shear fracture.

**Key words**: friction stir welded; mechanical property; fracture analysis

**The current cycle control of AC short circuit transition welding method and system** GU Jinmao, HUANG Pengfei, LU Zhenyang, YIN Shuyan (College of Mechanical Engineering & Applied Electronics Technology, Beijing University of Technology, Beijing 100124, China). p73—76

**Abstract**: A novel AC shortcircuit tansfer was presented.